PTEP

Prog. Theor. Exp. Phys. **2026** 033F01 (11 pages)
DOI: 10.1093/ptep/ptag025

Charge–Sign Dependent Drift Effects in the Time–Lag of Cosmic–Ray Variation Relative to Solar Activity Observed with the Calorimetric Electron Telescope (CALET)

O. Adriani [1,2], Y. Akaike [3,4], K. Asano [5], Y. Asaoka [5], E. Berti [2,6], P. Betti [2,6], G. Bigongiari [7,8], W. R. Binns [9], L. W. Blum[10], M. Bongi [1,2], P. Brogi [7,8], A. Bruno [11,12], N. Cannady [13], G. Castellini [6], C. Checchia [7,8], M. L. Cherry [14], G. Collazuol [15,16], G. A. de Nolfo [11], K. Ebisawa [17], A. W. Ficklin [14], H. Fuke [17], S. Gonzi [1,2,6], T. G. Guzik [14,†], T. Hams[18], K. Hibino[19], M. Ichimura [20], M. H. Israel [9], K. Kasahara [21], J. Kataoka [22], R. Kataoka [23], Y. Katayose [24], C. Kato [25], Y. Kato[26], N. Kawanaka [27,28], Y. Kawakubo [29], K. Kobayashi[3,4], K. Kohri [28,30], H. S. Krawczynski [9], J. F. Krizmanic [13], P. Maestro [7,8], P. S. Marrocchesi [7,8], M. Mattiazzi[15,16], A. M. Messineo [8,31], J. W. Mitchell[13], S. Miyake [32], A. A. Moiseev [13,33,34], M. Mori [35], N. Mori [2], H. M. Motz [36], K. Munakata [25,*], S. Nakahira [17], M. Negro [14], J. Nishimura[17], S. Okuno[19], J. F. Ormes [37], S. Ozawa [38], L. Pacini [2,6], P. Papini [2], A. Picquenot [14], B. F. Rauch [9], S. B. Ricciarini [2,6], K. Sakai[39], T. Sakamoto [29], M. Sasaki [13,33,34], Y. Shimizu[19], A. Shiomi [40], P. Spillantini[1], F. Stolzi [7,8], S. Sugita[29], M. Takita [5], T. Tamura[19], M. Teramoto [41], T. Terasawa [5], S. Torii [3], Y. Tsunesada [42,43], Y. Uchihori[44], E. Vannuccini [2], J. P. Wefel[14,†], K. Yamaoka [45], S. Yanagita [46,†], A. Yoshida[29], K. Yoshida [21], W. V. Zober [9], CALET Collaboration

[1]*Department of Physics, University of Florence, Via Sansone, 1-50019, Sesto Fiorentino, Italy*
[2]*L'Istituto Nazionale di Fisica Nucleare (INFN) Sezione di Firenze, Via Sansone, 1-50019, Sesto Fiorentino, Italy*
[3]*Waseda Research Institute for Science and Engineering, Waseda University, 17 Kikuicho, Shinjuku, Tokyo 162-0044, Japan*
[4]*Space Environment Utilization Center, Human Spaceflight Technology Directorate, Japan Aerospace Exploration Agency, 2-1-1 Sengen, Tsukuba, Ibaraki 305-8505, Japan*
[5]*Institute for Cosmic Ray Research, The University of Tokyo, 5-1-5 Kashiwa-no-Ha, Kashiwa, Chiba 277-8582, Japan*
[6]*Institute of Applied Physics (IFAC), National Research Council (CNR), Via Madonna del Piano, 10, 50019, Sesto Fiorentino, Italy*
[7]*Department of Physical Sciences, Earth and Environment, University of Siena, via Roma 56, 53100 Siena, Italy*
[8]*L'Istituto Nazionale di Fisica Nucleare (INFN) Sezione di Pisa, Polo Fibonacci, Largo B. Pontecorvo, 3-56127 Pisa, Italy*
[9]*Department of Physics and McDonnell Center for the Space Sciences, Washington University, One Brookings Drive, St. Louis, MO 63130-4899, USA*
[10]*Laboratory for Atmospheric and Space Physics, University of Colorado Boulder, Boulder, CO, USA*
[11]*Heliospheric Physics Laboratory, National Aeronautics and Space Administration (NASA)/Goddard Space Flight Center (GSFC), Greenbelt, MD 20771, USA*
[12]*Department of Physics, Catholic University of America, Washington, DC, USA*
[13]*Astroparticle Physics Laboratory, National Aeronautics and Space Administration (NASA)/Goddard Space Flight Center (GSFC), Greenbelt, MD 20771, USA*
[14]*Department of Physics and Astronomy, Louisiana State University, 202 Nicholson Hall, Baton Rouge, LA 70803, USA*

[15]*Department of Physics and Astronomy, University of Padova, Via Marzolo, 8, 35131 Padova, Italy*
[16]*L'Istituto Nazionale di Fisica Nucleare (INFN) Sezione di Padova, Via Marzolo, 8, 35131 Padova, Italy*
[17]*Institute of Space and Astronautical Science, Japan Aerospace Exploration Agency, 3-1-1 Yoshinodai, Chuo, Sagamihara, Kanagawa 252-5210, Japan*
[18]*Center for Space Sciences and Technology, University of Maryland, Baltimore County, 1000 Hilltop Circle, Baltimore, MD 21250, USA*
[19]*Kanagawa University, 3-27-1 Rokkakubashi, Kanagawa-ku, Yokohama, Kanagawa 221-8686, Japan*
[20]*Faculty of Science and Technology, Graduate School of Science and Technology, Hirosaki University, 3, Bunkyo, Hirosaki, Aomori 036-8561, Japan*
[21]*Department of Electronic Information Systems, Shibaura Institute of Technology, 307 Fukasaku, Minuma, Saitama 337-8570, Japan*
[22]*School of Advanced Science and Engineering, Waseda University, 3-4-1 Okubo, Shinjuku, Tokyo 169-8555, Japan*
[23]*Okinawa Institute of Science and Technology, 1919-1 Tancha, Onna-son, Kunigami-gun, Okinawa 904-0495, Japan*
[24]*Division of Intelligent Systems Engineering, Faculty of Engineering, Yokohama National University, 79-5 Tokiwadai, Hodogaya, Yokohama 240-8501, Japan*
[25]*Faculty of Science, Shinshu University, 3-1-1 Asahi, Matsumoto, Nagano 390-8621, Japan*
[26]*Department of Geophysics, Graduate School of Science, Tohoku University, 6-3 Aramaki-Aza-Aoba, Aoba-ku, Sendai, Miyagi 980-8578, Japan*
[27]*Department of Physics, Graduate School of Science, Tokyo Metropolitan University, 1-1 Minamii-Osawa, Hachioji, Tokyo 192-0397, Japan*
[28]*National Astronomical Observatory of Japan, 2-21-1 Osawa, Mitaka, Tokyo 181-8588, Japan*
[29]*Department of Physical Sciences, College of Science and Engineering, Aoyama Gakuin University, 5-10-1 Fuchinobe, Chuo, Sagamihara, Kanagawa 252-5258, Japan*
[30]*Institute of Particle and Nuclear Studies, High Energy Accelerator Research Organization (KEK), 1-1 Oho, Tsukuba, Ibaraki 305-0801, Japan*
[31]*University of Pisa, Polo Fibonacci, Largo B. Pontecorvo, 3-56127 Pisa, Italy*
[32]*Department of Electrical and Computer Engineering, National Institute of Technology (KOSEN), Gifu College, 2236-2 Kamimakuwa, Motosu-city, Gifu 501-0495, Japan*
[33]*Center for Research and Exploration in Space Sciences and Technology, National Aeronautics and Space Administration (NASA)/Goddard Space Flight Center (GSFC), Greenbelt, MD 20771, USA*
[34]*Department of Astronomy, University of Maryland, College Park, MD 20742, USA*
[35]*Department of Physical Sciences, College of Science and Engineering, Ritsumeikan University, Shiga 525-8577, Japan*
[36]*Faculty of Science and Engineering, Global Center for Science and Engineering, Waseda University, 3-4-1 Okubo, Shinjuku, Tokyo 169-8555, Japan*
[37]*Department of Physics and Astronomy, University of Denver, Physics Building, Room 211, 2112 East Wesley Avenue, Denver, CO 80208-6900, USA*
[38]*Quantum ICT Advanced Development Center, National Institute of Information and Communications Technology, 4-2-1 Nukui-Kitamachi, Koganei, Tokyo 184-8795, Japan*
[39]*Kavli Institute for Cosmological Physics, The University of Chicago, 5640 South Ellis Avenue, Chicago, IL 60637, USA*
[40]*College of Industrial Technology, Nihon University, 1-2-1 Izumi, Narashino, Chiba 275-8575, Japan*
[41]*Department of Electrical Engineering, Kyushu Institute of Technology, 1-1 Sensui-cho, Tobata-ku, Kitakyushu, Fukuoka, Japan*
[42]*Graduate School of Science, Osaka Metropolitan University, Sugimoto, Sumiyoshi, Osaka 558-8585, Japan*
[43]*Nambu Yoichiro Institute for Theoretical and Experimental Physics, Osaka Metropolitan University, Sugimoto, Sumiyoshi, Osaka 558-8585, Japan*
[44]*National Institutes for Quantum and Radiation Science and Technology, 4-9-1 Anagawa, Inage, Chiba 263-8555, Japan*
[45]*Nagoya University, Furo, Chikusa, Nagoya 464-8601, Japan*
[46]*College of Science, Ibaraki University, 2-1-1 Bunkyo, Mito, Ibaraki 310-8512, Japan*

Received December 5, 2025; Revised January 28, 2026; Accepted January 29, 2026; Published February 17, 2026

The 11-yr variation of galactic cosmic-ray flux lags behind the variation of the sunspot number. An average ∼1-yr time-lag is expected from the outward propagating solar wind with the frozen-in photospheric magnetic field varying in the solar cycle, and from the inward diffusive transport of cosmic-ray particles. The long-term neutron monitor data, however, show that the time-lag is significantly longer (shorter) in the odd (even) solar cycle. In this paper, we analyze the time-lag in proton and electron fluxes observed by the Calorimetric Electron Telescope (CALET). It is found that the time-lag is similar in proton and electron fluxes during an $A > 0$ polarity epoch of the solar dipole magnetic field. In an even solar cycle 24 including a polarity reversal from $A < 0$ to $A > 0$, on the other hand, it is found that the time-lag of proton (electron) flux variation is significantly shorter (longer) than the average ∼1-yr lag by analyzing the combined data with CALET and AMS-02. This is the first observation of the charge-sign dependent time-lag. We demonstrate that these observations can be qualitatively interpreted in terms of different 11-yr time profiles of proton and electron fluxes in $A > 0$ and $A < 0$ epochs expected from the drift effect.

Subject Index F01

1. Introduction

The galactic cosmic ray (GCR) intensity observed at Earth shows a clear ∼11-yr cycle variation in an anticorrelation with the solar activity as a result of the large-scale GCR transport in the heliosphere. The potential importance of the gradient and curvature drift in the GCR transport was first addressed theoretically by Ref. [1]. The drift effect results in an anticorrelation between the GCR intensity at Earth and the tilt angle of the heliospheric current sheet (HCS), which increases with the solar activity [2–7]. Since the orientation of the guiding center drift reverses according to the alteration of the sign (q) of the particle's charge and the sign (A) of the solar dipole magnetic field polarity, the drift model predicts different amplitudes of anticorrelation between the GCR intensity and the HCS tilt angle for $qA > 0$ and $qA < 0$. During periods with $A > 0$, the solar polar magnetic field is directed away from (toward) the Sun in the northern (southern) hemisphere, and the drift effect leads electrons ($q < 0$) propagating inward toward the Earth along the HCS while the distance along the access route becomes longer as HCS waviness increases. The drift effect, on the other hand, leads protons ($q > 0$) to arrive at Earth from the heliospheric polar region, accessing the HCS less often. This results in a larger modulation amplitude of the electron flux than that of the proton flux at Earth while the HCS tilt angle increases in the $A > 0$ epoch. This is seen in the "peaked" and "broad" maxima of ∼11-yr GCR variations when $qA < 0$ or $qA > 0$, respectively. These time profiles have been observed in protons and electrons measured at the same average rigidity by the Calorimetric Electron Telescope (CALET) onboard the International Space Station and successfully reproduced by a numerical drift model [8].

This paper clarifies the drift effect seen in the time-lag of the long-term temporal variation of GCR proton and electron fluxes behind that of the sunspot number (SSN), which is an index of solar activity. About a 1-yr lag is expected from the outward propagating solar wind with the frozen-in photospheric magnetic field, which varies in the solar cycle (SC), and from the inward diffusive transport of GCR particles, which is affected by the large-scale drift in the heliosphere.

*kmuna00@shinshu-u.ac.jp
†Deceased.

Based on the long-term record of neutron monitors (NMs), however, many papers have reported that the lag is significantly longer (shorter) in the odd (even) SCs [9–13]. For instance, Tomassetti et al. [13] reported that the lag is ∼12 (∼3) months in odd (even) SCs while the mean lag is about 8 months. NMs measuring primary GCR nuclei with $q > 0$ observe the "transition" from $A < 0$ to $A > 0$ ($A > 0$ to $A < 0$) in the even (odd) SC, which occurs according to the polarity reversal of the solar dipole magnetic field at the solar maximum. Although this indicates that the drift effect is somehow responsible for the observed asymmetry between time-lags in odd and even cycles, no comprehensive interpretation of the asymmetry has been proposed yet.

To analyze the drift effect using observations with NMs that respond to GCR nuclei with $q > 0$ alone, we need observations in both $A > 0$ and $A < 0$ epochs. In such an analysis with data observed in different time periods, however, it is generally difficult to distinguish the difference due to the drift effect for $qA > 0$ and $qA < 0$ from the difference due to other modulation parameters. For example, modulation parameters including the SSN, the solar wind velocity, and the magnetic field strength are all generally different in different time periods. By using simultaneous observations of GCRs with $q > 0$ and $q < 0$, on the other hand, we can analyze the difference from data only in an $A > 0$ or $A < 0$ epoch alone. In the next section, we analyze the lag of GCR variation behind the SSN variation by using observations with the CALET.

2. Data and analyses

2.1. *Proton and electron count rates observed by CALET*

The normal event trigger of CALET is always carried out by the high-energy trigger with an energy threshold of ∼10 GeV. In addition to this high-energy trigger, in order to collect the low-energy ($\gtrsim$1 GeV) particle events efficiently, a low-energy electron (LEE) trigger is used at high geographical latitudes where the geomagnetic cutoff rigidity (COR) is below 5.0 GV. This LEE shower trigger mode is operated for 90 s twice per International Space Station orbital period (∼91 minutes), at a 51.6° orbital inclination, in each of the north and south regions. In this paper, we have analyzed the flight data collected in the LEE trigger mode during 10 years between 2015 and 2024. We have collected about 1.5×10^8 low-energy GCR candidates in a total observational live time of approximately 1367 h. From this dataset, we select electrons and protons and deduce their count rates for the same average rigidity. For details of the detector configuration of CALET and selection criteria for protons and electrons, readers can refer to our earlier paper [8].

In order to minimize the count rate variation due to the COR variation, we choose periods in which COR is below 0.8 GV and select events recorded with the total deposited energy exceeding 1.0 GeV. The COR is calculated by back-tracing the particle's trajectory in the magnetosphere defined by the IGRF-13 [14] and TS05 [15] empirical models [16] for every incident direction. Orbit calculations are repeated by decreasing the particle's rigidity, and the COR is defined as the lowest rigidity before the appearance of the penumbra.[1] For the analysis of the charge-sign dependent solar modulation in this paper, we derive the count rates of electrons and protons at

[1] Penumbra refers to the rigidity interval in which trajectory tracing through the Earth's magnetic field yields a mixture of allowed and forbidden access directions for interplanetary cosmic rays.

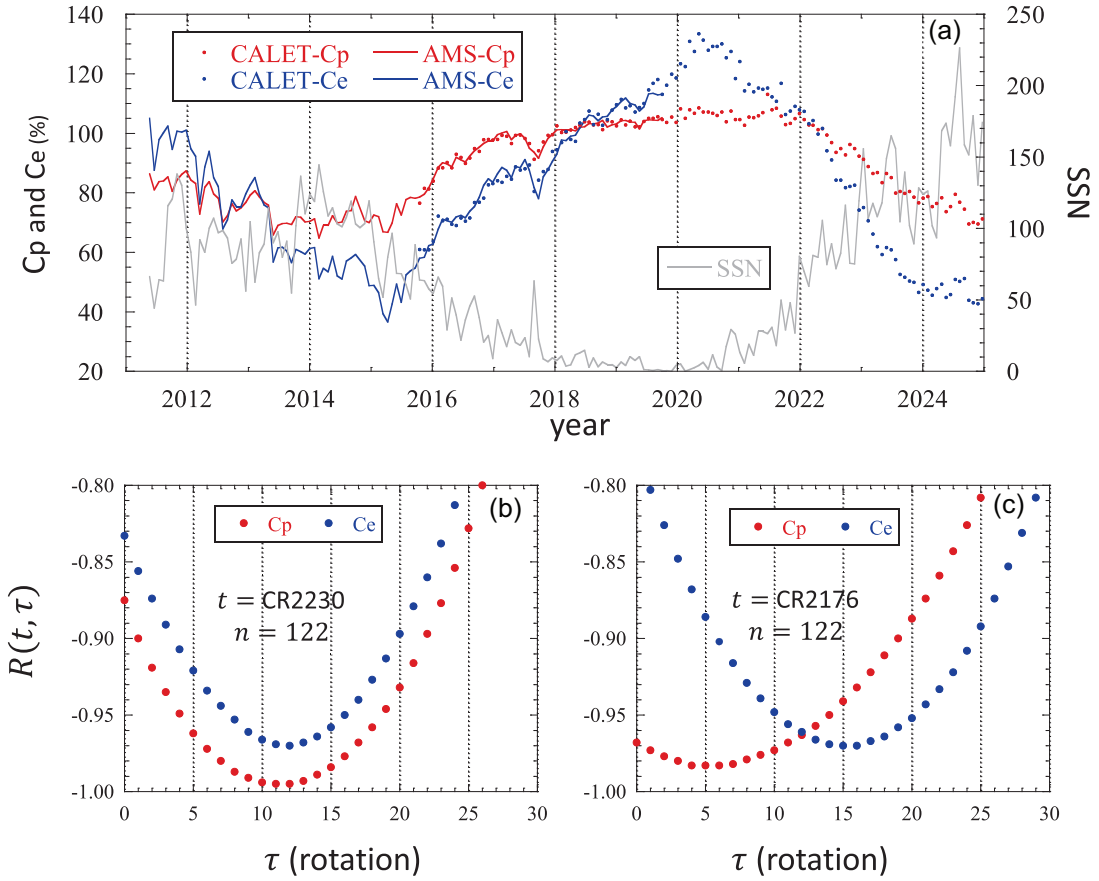

Fig. 1. Normalized count rates of protons and electrons observed by CALET. (a) Red and blue filled circles display the rotation averages of proton (C_p) and electron (C_e) count rates at the average rigidity of 3.8 GV, whereas red and blue solid curves display C_p and C_e reproduced from the daily fluxes given by AMS-02 in rigidity ranges 3.64–4.02 GV and 2.97–4.02 GV, respectively (see text) [17,18]. C_p and C_e by CALET are observed in 124 CRs between CR2169 (October 2015) and CR2292 (December 2024), whereas C_p and C_e by AMS-02 are observed in 113 CRs between CR2110 (May 2011) and CR2222 (September 2019). Averages of C_p and C_e over 76 rotations between CR2169 and CR2244 are normalized to 100. (b) $R(t, \tau)$ calculated by Eq. (1) at t = CR2230 with $n = 122$ CRs (CR2169–CR2291) covering the $A > 0$ epoch. (c) $R(t, \tau)$ at t =CR2176 with $n = 122$ CRs (CR2115–CR2237) covering ∼82% of the SC 24.

the same average rigidity. The average rigidity of electrons that passed the selection criteria is estimated to be ∼3.8 GV from Monte Carlo (MC) simulations, whereas the average rigidity of protons is adjusted to ∼3.8 GV by selecting the events for which the energy deposit in all layers of the IMC (IMaging Calorineter) and the TASC (Total AbSorption Calorimeter) is between 1 and 3 GeV, which is verified from MC simulations. We analyze about 1.18×10^6 electron and 2.05×10^6 proton candidates collected in the same total observational live time of about 339 h.

Filled circles in Fig. 1(a) show time profiles of the normalized count rates of protons C_p (red) and electrons C_e (blue) with the same average rigidity of 3.8 GV observed by CALET over the 10-year period from 2015 to 2024. In this figure, the average count rate over 6 years between 2015 and 2021 is normalized to 100 and each circle shows an average within a solar rotation (Carrington rotation: CR) period, which is about 27 days. Also shown by a gray curve on the right vertical axis is the CR average of the SSN, which is calculated from the daily mean value (https://doi.org/10.24414/qnza-ac80). The observation by CALET covers an $A > 0$ epoch fol-

lowing the solar maximum in 2014. The C_p of protons (C_e of electrons) count rate clearly shows the "broad" ("peaked") maximum in the $A > 0$ epoch, as reproduced by our numerical drift model [8]. The amplitude of the ∼11-yr variation of C_e is significantly larger than that of C_p even at the same average rigidity. A similar feature is also observed by AMS-02 between 2011 and 2020 [17,18]. This is due to the drift effect in which a stronger anticorrelation between the GCR intensity and the HCS tilt angle results for $qA < 0$ than for $qA > 0$.

2.2. *Time-lag of the GCR count rate variation behind the SSN*

By calculating the cross-correlation coefficient, we derive the time-lag of GCR variation behind the SSN variation. Let $x(t_i)$ and $y(t_i)$ be the SSN and GCR count rate at a time t_i of the i-th rotation, respectively. We calculate the Pearson's cross-correlation coefficient R at t, as

$$R(t,\tau) = \frac{\sum_{t_i=t-n/2}^{t+n/2}\{x(t_i)-\bar{x}(t)\}\{y(t_i+\tau)-\bar{y}(t,\tau)\}}{\sqrt{\sum_{t_i=t-n/2}^{t+n/2}\{x(t_i)-\bar{x}(t)\}^2\sum_{t_i=t-n/2}^{t+n/2}\{y(t_i+\tau)-\bar{y}(t,\tau)\}^2}},$$
$$\bar{x}(t) = \frac{1}{n+1}\sum_{t_i=t-n/2}^{t+n/2} x(t_i), \quad \bar{y}(t,\tau) = \frac{1}{n+1}\sum_{t_i=t-n/2}^{t+n/2} y(t_i+\tau), \tag{1}$$

where τ is the time-lag in rotation number and $n+1$ is the total number of rotations used for the summation. In this equation, we use the central moving averages of SSN, C_p, and C_e in Fig. 1(a) each over 13 rotations to minimize the influence of short-term variations and calculate $R(t,\tau)$ by changing τ from −30 to +30 rotations in every 1 rotation step. Filled circles in Fig. 1(b) show the calculated $R(t,\tau)$s at t =CR2230 (in May 2020) with $n = 122$ CRs covering the $A > 0$ epoch in 2015–2024 (CR2169–CR2291) for protons ($y(t) = C_p(t)$) (red) and electrons ($y(t) = C_e(t)$) (blue), each as a function of τ. We find the time-lag ($\tau_{\max}$) giving the maximum $|R(t,\tau)|$ is almost similar in the $A > 0$ epoch, i.e. 11 rotations (∼10 months) and 12 rotations (∼11 months) for C_p and C_e, respectively.

We next validate the time-lag asymmetry in the "even" and "odd" SCs. If this asymmetry is due to the charge-sign dependent drift effect, an asymmetry is also expected between time-lags of C_p and C_e in a single "even" (or "odd") SC. The CALET observation, however, covers only a half-period of the "even" SC 24 between 2009 and 2019. Therefore, we extend the observation period back to 2011 by combining the published AMS-02 data with the CALET data in Fig. 1(a). From the daily mean proton and electron fluxes in rigidity ranges 3.64–4.02 GV and 2.97–4.02 GV, respectively, published by AMS-02, we calculate CR averages [17,18]. Figure 2 shows the correlation between proton [Fig. 2(a)] and electron [Fig. 2(b)] count rates by the CALET and AMS-02 during a period between 2015 and 2019 when two observations are overlapping. In this figure, the average flux observed by AMS-02 over an entire period between 2011 and 2019 is normalized to 100. A good correlation with the correlation coefficient exceeding +0.98 is seen in each of the proton and electron count rates. Therefore, we convert proton and electron fluxes by AMS-02 to C_p and C_e by CALET, respectively, by using the linear regression equation indicated in each panel. Red and blue solid curves in Fig. 1(a) display the converted proton and electron count rates, respectively. By this extension of the observation period, C_p and C_e become available in a period between 2011 and 2020 (CR2115–CR2237) covering ∼82% of the solar SC 24. All data used for the time-lag analysis in this paper can be found in the Supplementary Data.

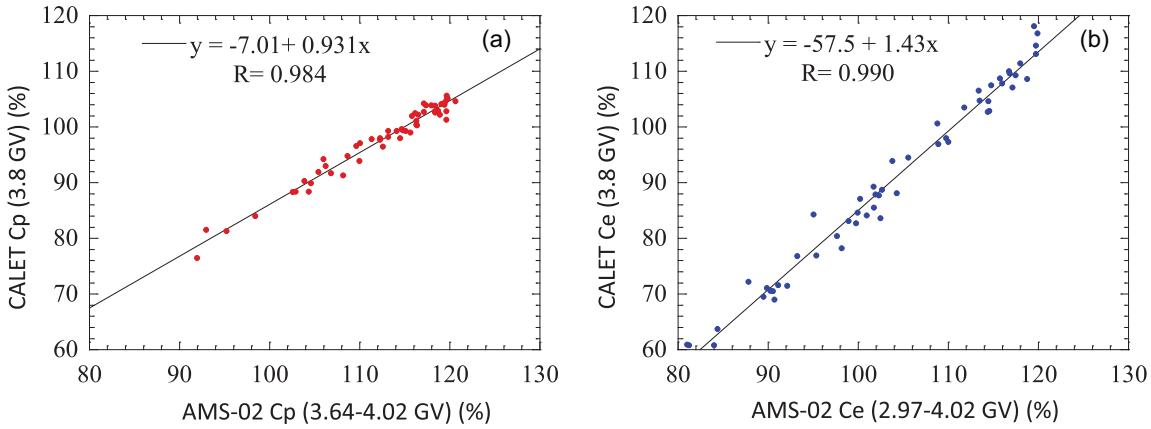

Fig. 2. Correlation between the normalized count rates observed by CALET and the normalized fluxes by AMS-02 over 54 CRs between CR2169 (October 2015) and CR2222 (September 2019) when two observations overlapped [see Fig. 1(a)] [17,18]. (a) Correlation of C_p, (b) correlation of C_e. The best-fit linear equation and Pearson's correlation coefficient (R) are indicated in each panel.

Figure 1(c) displays $R(t, \tau)$ at $t =$ CR2176 (in April 2016) with $n = 122$ CRs in the SC 24 in the same format as Fig. 1(b). A significant charge-sign dependence is seen in $\tau_{\max}$ in this figure, i.e. $\tau_{\max}$ is only 5 rotations (∼4.5 months) for protons whereas it is 15 rotations (∼13.5 months) for electrons. This is the first observation of the charge-sign dependent time-lag between the GCR count rate and the SSN. Note that the "even" SC 24 includes the transition from the $A < 0$ epoch to the $A > 0$ epoch at the solar maximum around 2014. Therefore, the shorter time-lag of the proton ($q > 0$) count rate occurred in the SC including the transition from $qA < 0$ to $qA > 0$, whereas the longer time-lag of the electron ($q < 0$) count rate occurred in the SC including the $qA > 0$ to $qA < 0$ transition. This is consistent with the asymmetric time-lag in "even" and "odd" cycles reported from the long-term observations with NMs, which respond to GCR nuclei with positive charge ($q > 0$).

The gradient–curvature drift velocity (v_D) scales schematically as $v_D \propto R \times (v/c)$, so mass enters only implicitly via the momentum–speed relation. However, although at lower rigidities mass-dependent effects via v/c, scattering, and transport coefficients can be important, at the mean rigidity relevant to our analysis (∼3.8 GV) both positrons and protons are essentially relativistic and the residual species dependence introduced by the v-factor is weak. Consequently, in a guiding center drift picture the dominant controls at these rigidities are rigidity and charge sign rather than rest mass, and a purely drift-based model does not predict a substantially larger time-lag for positrons than for protons. Charge-dependent differences instead arise primarily from the drift geometry, which determines the effective propagation path length L. During the $A < 0$ epoch of SC 24 positively charged particles drift inward predominantly along the HCS, producing a longer effective L than for negatively charged particles; this geometry, rather than particle mass, governs the relative time-lag behavior. The AMS-02 results report charge-sign dependent time variations across 1–50 GeV and are qualitatively consistent with this interpretation [19]. Quantitative agreement on lag magnitudes, however, requires full transport modeling that includes drift together with diffusion, convection, and adiabatic effects.

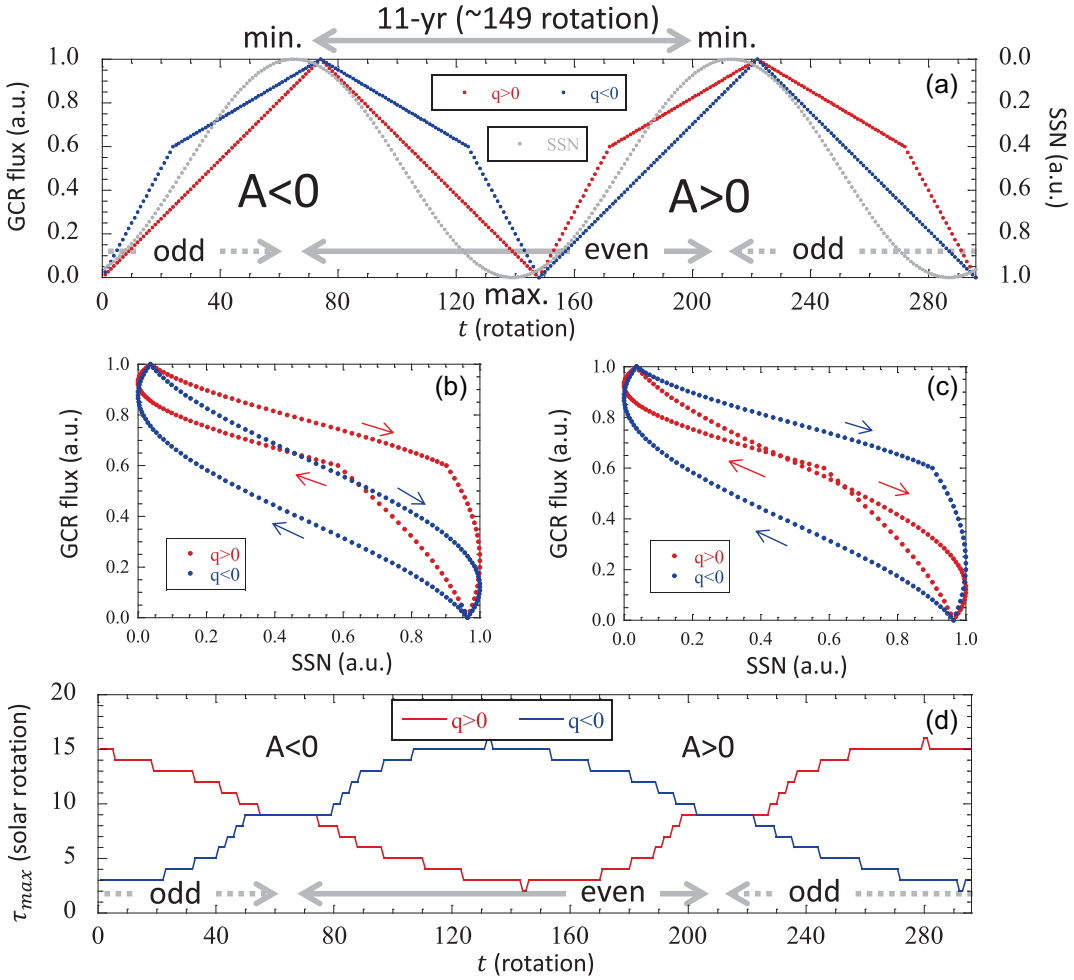

Fig. 3. Schematic illustration of long-term variations of GCR fluxes expected from the drift effect. (a) The red and blue curves display the variations of GCRs with positive ($q > 0$) and negative ($q < 0$) charges, respectively, in successive $A < 0$ and $A > 0$ epochs, whereas the gray curve shows the variation of the SSN on the right vertical axis. The phase of the gray curve is advanced for 9 rotations relative to the red and blue curves to represent the observed mean time-lag of GCR flux behind the SSN. Note that the vertical scale of SSN variation is inverted to make it easier to see the time-lag of the red and blue curves. The time t on the horizontal axis is in units of the solar rotation period (~27 days). Within T =11-yr, the gray curve is calculated as a function of t as $0.5 \times \cos\{2\pi(t + 9\ \text{CRs})/T\} + 0.5$. Blue and red curves for $qA < 0$ are calculated as two straight lines connecting three points at $(X, Y) = (0, 0)$, $(T/2, 1.0)$, and $(T, 0)$, whereas curves for $qA > 0$ are calculated as four lines connecting (0,0), $(T/6, 0.6)$, $(T/2, 1.0)$, $(5T/6, 0.6)$, and $(T, 0)$. (b) The correlation between GCR flux and SSN in panel (a) in the $A > 0$ epoch, (c) the correlation in an even SC including $A < 0$ to $A > 0$ polarity reversal at the solar maximum. Each data circle in panels (b) and (c) tracks the red or blue loop clockwise in time, as indicated by red and blue arrows. (d) $\tau_{\max}$ giving the maximum $|R(t, \tau)|$ as a function of t. $R(t, \tau)$ is calculated by Eq. (1) using GCR flux and SSN in panel (a) for y and x, respectively.

3. Discussions and summary

In this section, we discuss how the observed charge-sign dependent time-lags can be interpreted in terms of the drift effect. Red and blue curves in Fig. 3(a) schematically display the simulated variation of fluxes of GCRs with positive ($q > 0$) and negative ($q < 0$) charges, respectively, in successive $A < 0$ and $A > 0$ epochs, each spanning 11 years. The red (blue) curve in the $A > 0$ epoch mimics the observed time profile of C_p (C_e) with a "broad" ("peaked") maximum

in Fig. 1(a). The drift model predicts that time profiles of red and blue curves switch in the $A < 0$ epoch. Although the observed amplitude of variation in Fig. 1(a) is different in C_p and C_e, all amplitudes in Fig. 3(a) are normalized to 1.0 because the variation amplitude does not alter the time-lag behind the SSN discussed here. The horizontal axis is time in units of the solar rotation period (27 days) and 11 years corresponds to 149 rotations. Also shown by the gray curve is the 11-yr variation of the SSN simulated by a sinusoidal function of time. The phase of the gray curve is advanced for 9 rotations relative to the red and blue curves to represent the observed mean time-lag of GCR flux behind the SSN. Note that the vertical scale of SSN variation on the right axis is inverted to make it easier to see the time-lag of red and blue curves relative to the gray curve.

In the present work, Fig. 3(a) is used solely as a qualitative illustration to interpret the charge-sign dependent time-lag shown in Fig. 1(b–c), which is the main result of the paper. The functional forms used for the curves are provided in the caption. For our purposes, the essential feature is that C_p increases (decreases) earlier than C_e during the descending (ascending) phase of the solar activity in the $A > 0$ epoch. This relative timing, rather than the detailed shape of the peak, is what drives the qualitative interpretation of the observed time-lag.

Red (blue) filled circles in Fig. 3(b) show the correlation between the red (blue) curve in Fig. 3(a) on the y-axis and the gray curve on the x-axis in the $A > 0$ epoch, whereas Fig. 3(c) displays the correlation in SC 24. Due to the lag of the GCR variation behind the SSN variation, each data circle in this figure traces a loop clockwise in time as indicated by red and blue arrows in Fig. 3(b) and 3(c), and the loop width reflects the magnitude of the lag. This loop is known as the "hysteresis" curve. It is seen in Fig. 3(a) in the $A > 0$ epoch that the red and blue loops have a similar width, indicating a similar time-lag ($\tau_{\max}$) for $q > 0$ and $q < 0$. This is qualitatively consistent with the observed $\tau_{\max}$ in Fig. 1(b). In contrast, in Fig. 3(c) displaying the correlation during the even SC between two solar minima, the blue loop is much wider than the red loop, indicating a significantly larger time-lag for $q < 0$ than that for $q > 0$. This is also qualitatively consistent with the observed $\tau_{\max}$ in Fig. 1(c).

Loop features in Fig. 3(b) and 3(c) can be qualitatively interpreted from the illustrated time profiles in Fig. 3(a) as follows. During 11 years, the GCR flux for $qA < 0$ monotonically increases (decreases) toward (after) a maximum at the solar minimum. Due to this, the average time-lag of the blue curve ($q < 0$) relative to the gray curve in the $A > 0$ epoch becomes close to the assumed mean lag of 9 rotations. The GCR flux for $qA > 0$, on the other hand, rapidly increases (decreases) after (before) the solar maximum, resulting in short (long) lag before (after) the solar minimum. Thus, the average time-lag of the red curve ($q > 0$) relative to the gray curve also becomes close to the mean of 9 rotations in the $A > 0$ epoch. This qualitatively explains the similar width of the red and blue loops in Fig. 3(b) and the similar $\tau_{\max}$ in Fig. 1(b). In the even SC including the transition from the $A < 0$ epoch to the $A > 0$ epoch at the solar maximum, on the other hand, the lag of $q < 0$ GCR flux (blue curve) is long (mean 9 rotations) toward (after) the solar maximum, while the lag of $q > 0$ GCR flux (red curve) is mean 9 rotations (short) toward (after) the solar maximum. Thus, the average time-lag becomes long (short) for $q < 0$ ($q > 0$) in even SCs. This qualitatively explains the loop widths in Fig. 3(c) and $\tau_{\max}$ in Fig. 1(c).

We finally calculate $R(t, \tau)$ of Fig. 3(a) data by changing t and obtain $\tau_{\max}$ as a function of t. Figure 3(d) shows results. It is seen that $\tau_{\max}$ in the $A > 0$ epoch is about 9 rotations regardless of whether $q > 0$ or $q < 0$, in accord with the observation in Fig. 1(b). On the other hand, $\tau_{\max}$ for $q > 0$ ($q < 0$) in an odd (even) cycle is significantly longer than that in an even (odd) cycle.

At least qualitatively, $\tau_{\max}$ for $q > 0$ is also consistent with the time-lag asymmetry in odd and even cycles, such as reported by Koldobskiy et al. [12] and Tomassetti et al. [13] from long-term observations with NMs.

The asymmetry in $\tau_{\max}$ for $q > 0$ and $q < 0$ in an even SC results from the transition between the upper and lower loops in Fig. 3(b) at the solar maximum. Due to the transition from $qA < 0$ to $qA > 0$ in even SCs, $q < 0$ ($q > 0$) data transition from tracing the upper (lower) loop transfer to tracing the lower (upper) loop. Due to this transition, the loop becomes wider (narrower) for $q < 0$ ($q > 0$) as shown in Fig. 3(c). A similar idea of the transition between two loops had already been proposed in an early paper [10] to interpret the different time-lags observed by NMs in odd and even cycles. However, their model assumes the NM count rate at the solar minimum in $A > 0$ significantly higher than that in $A < 0$, in contradiction to the long-term observation. The drift model in Fig. 3(a), on the other hand, can reproduce the different time-lags even with the same GCR flux at $A > 0$ and $A < 0$ solar minima.

Although our results presented above are qualitatively consistent with drift effects, other heliospheric parameters such as solar wind speed, turbulence, and magnetic field strength may also influence the observed time–lags. Future work incorporating quantitative modeling of drift, diffusion, convection, and turbulence will be necessary to disentangle their relative contributions and provide a more comprehensive explanation of the observed time–lag behavior. For quantitative modeling of the time-lag, which is out of scope of the present paper though, we need to improve our drift model presented in Ref. [8], so that it can successfully reproduce the observed profiles of C_p and C_e including the polarity reversal period at the solar maxima.

In summary, we reported the time-lag of the GCR intensity variation behind the SSN by analyzing proton and electron count rates observed at the same average rigidity with CALET. It is found with CALET that the lags in the $A > 0$ epoch, 2015–2024, are similar for both proton and electron count rates (11 and 12 rotations for proton and electrons, respectively). In contrast, the lag in the even solar SC 24 between 2009 and 2019, obtained with both of CALET and AMS-02, is only 5 rotations for protons, whereas it is 15 rotations for electrons. This is the first observation of the charge-sign dependent time-lag between the GCR count rate and the SSN. It is demonstrated that these observations can be qualitatively interpreted in terms of the GCR time profile with a "broad" ("peaked") maximum expected from the drift effect in the $qA > 0$ ($qA < 0$) condition.

Acknowledgements

We gratefully acknowledge the Japan Aerospace Exploration Agency (JAXA)'s contributions to the development of CALET and to the operations aboard the Japanese Experiment Module—Exposed Facility (JEM-EF) on the International Space Station. We also express our sincere gratitude to Agenzia Spaziale Italiana (ASI) and the National Aeronautics and Space Administration (NASA) for their support of the CALET project.

Supplementary material

Supplementary material is available at *PTEPHY* online.

Funding

This work was supported in part by Japan Society for the Promotion of Science (JSPS) Grant-in-Aid for Scientific Research (S) No. 26220708, No. 19H05608, and No. 24H00025, JSPS Grant-in-Aid for Scientific Research (B) No. 24K00665, and by the Ministry of Education, Culture, Sports, Science and Technology (MEXT) Supported Program for the Strategic Research Foundation at Private Universities (2011–2015) (No. S1101021) at Waseda University. The CALET effort in Italy is supported by ASI under Agreement No. 2013-018-R.0 and its amendments. The CALET effort in the United States is supported by NASA through Grants No. NNX16AB99G, No. NNX16AC02G, and No. NNH14ZDA001N-APRA-0075.

Data availability

All data used in this study are available from the Supplementary Data.

References

[1] J. R. Jokipii, E. H. Levy, and W. B. Hubbard, Astrophys. J. **213**, 861 (1977).
[2] J. R. Jokipii and B. Thomas, Astrophys. J. **243**, 1115 (1981).
[3] J. Kóta and J. R. Jokipii, Astrophys. J. **265**, 573 (1983).
[4] M. Garcia-Munoz, P. Meyer, K. R. Pyle, J. A. Simpson, and P. Evenson, J. Geophys. Res. **91**, 2858 (1986).
[5] V. Di Felice, R. Munini, E. E. Vos, and M. S. Potgieter, Astrophys. J. **834**, 89 (2017).
[6] O. P. M. Aslam, M. S. Potgieter, X. Luo, and M. D. Ngobeni, Astrophys. J. **947**, 72 (2023).
[7] M. Potgieter, Living Rev. Solar Phys. **10**, 3 (2013).
[8] O. Adriani et al. [CALET Collaboration], Phys. Rev. Lett. **130**, 211001 (2023).
[9] H. Moraal, Space Sci. Rev. **19**, 845 (1976).
[10] K. Nagashima and I. Morishita, Planet. Space Sci. **28**, 195 (1980).
[11] I. G. Usoskin, K. Mursula, H. Kananen, and G. A. Kovaltsov, Adv. Space Res. **27**, 571 (2001).
[12] S. A. Koldobskiy, R. Kähkönen, B. Hofer, N. A. Krivova, G. A. Kovaltsov, and I. G. Usoskin, Solar Phys. **297**, 38 (2022).
[13] N. Tomassetti, B. Bertucci, and E. Fiandrini, Phys. Rev. D. **106**, 103022 (2022).
[14] P. Alken et al., Earth Planets Space **73**, 49 (2021).
[15] N. A. Tsyganenko and M. I. Sitnov, J. Geophys. Res. **110**, A03208 (2005).
[16] S. Miyake, R. Kataoka, and T. Sato, Space Weather **15**, 589 (2017).
[17] M. Aguilar et al. [AMS Collaboration], Phys. Rev. Lett. **127**, 271102 (2021).
[18] M. Aguilar et al. [AMS Collaboration], Phys. Rev. Lett. **130**, 161001 (2023).
[19] M. Aguilar et al. [AMS Collaboration], Phys. Rev. Lett. **121**, 051102 (2018).